Determining non-stationary state of solid-propellant rocket engine model based on numerical conjugate problem solution

Determining non-stationary state of solid-propellant rocket engine model based on numerical conjugate problem solution

A P Zhukov, S V Belov, S V Ponomarev

National Research Tomsk State University, 36 Lenin Avenue, Tomsk, 634050,Russia

E-mail: zh@niipmm.tsu.ru

Abstract. This paper describes the solid-propellant rocket engine structure, including casing and filler. The gas flows within the filler channel. Based on numerical conjugate problem solution, non-stationary stress-strain states of the casing and filler were determined, as well as gas flow parameters in the channel. Within the conjugate problem, the engine is considered to be a two-component system: deformable solid body and gas. Conjugate problem solution involves specific subtasks related to the conjugation conditions, where Lagrangian approach is used for subtasks of solid body. Euler approach is used for subtasks of gas, implying immovable boundary of the computational domain on the integration time step. Numerical methods are applied in solving subtasks. Specific feature of conjugate problem solution algorithm is discrete movable domain boundary interface.

1. Introduction

One type of conjugate problems could be considered as the interaction between fluid/gas flow and deformable solid body. In this problem formulation, there are at least two physical mediums. This interaction occurs on the boundary interface (BI) which is mathematically formulated on the basis of conjugation conditions i.e. continuity of such values as forces and velocities. Thus, BI mediums could be displaced and deformed.

Conjugate problem is subdivided according to physical processes [1]-[6]. In determining stress-strain state of a solid body, Lagrangian description involves movable boundaries naturally. The main issue in solving conjugate problem is the calculation fluid phase flow field taking into consideration movable boundary of the computational domain. At present time to solve such problems ALE (Arbitrary Lagrangian-Eulerian) methods are widely used [7]-[10]. They are based on combination of Lagrange and Euler descriptions.

However, the majority of numerical methods applied in calculating fluid phase flow field were based on the assumption that its boundaries are not movable (Euler description). On the basis of these methods, quite a number of successfully software programs were developed. To solve conjugate problem for solid-propellant rocket engine (SPRE) model, the algorithm is applied, where individual subtasks are solved on the basis of existing numerical methods and software program modules. It should be noted that in the program module Euler approach is applied for the gas medium phase. Input data of geometry and structure of space grids, initial and boundary conditions are applied in the independent computational modules of individual subtasks for every time integration step. Conjugate conditions are realized as data interchange between program modules. Under conditions of the conjugate problem, boundary motion of solid phase is continuous, while gas phase boundary motion is discrete. This implies that within specific time step the boundary is immovable, whereas its motion is

replaced by the gas injection from the boundary itself. In this case, the boundary motion becomes jump-wise excluding intermediate states which, in its turn, is determined by the solid body calculation results and conjugate conditions.

2. Problem statement

Let's consider compressible gas- solid body system. Gas occupies the domain $\Omega_G(t)$ within boundary $\partial\Omega_G(t)$, while solid body- $\Omega_S(t)$ within boundary $\partial\Omega_S(t)$. Domains Ω_G and Ω_S have common boundary Γ, where both mediums interact, whereas, $\Gamma=\partial\Omega_G\cap\partial\Omega_S$.

In the case of moving gas volume $\Omega_G(t)$ within boundary $\partial\Omega_G(t)$, conservation laws of mass, momentum, energy are:

$$\frac{d}{dt}\int\limits_{\Omega_G(t)}\mathbf{Q}d\Omega+\int\limits_{\partial\Omega_G(t)}\mathbf{Q}((\mathbf{v}-\mathbf{v}_b)\cdot\mathbf{n})dS+\int\limits_{\partial\Omega_G(t)}\mathbf{H}\cdot\mathbf{n}dS=0 \tag{1}$$

Vectors **Q** and **H** are:

$$\mathbf{Q}=\left(\rho,\quad \rho\mathbf{v},\quad e\right)^T,\ \mathbf{H}=\left(0,\quad -\boldsymbol{\tau},\quad P\mathbf{v}-\mathbf{q}\right)^T. \tag{2}$$

The following notations are applied in expressions (1) and (2): ρ_G – gas density; $\mathbf{v}=\{\upsilon_i\}$ – gas velocity vector, i=1,2,3; $\mathbf{v}_b=\left\{\upsilon_i^b\right\}$ – velocity vector for points of boundary $\partial\Omega_G$,; $\mathbf{n}$ – normal vector for boundary area element dS; P – pressure; $\boldsymbol{\tau}$ – stress tensor in gas and its components $\tau_{ij}=-P\delta_{ij}+\mu(\upsilon_{i,j}+\upsilon_{j,i})-\frac{2}{3}\mu(\upsilon_{k,k})\delta_{ij}$; $e=\rho\left(\varepsilon+\frac{\mathbf{v}^2}{2}\right)$ – total energy of volume unit, where $\varepsilon=\frac{P}{(\gamma-1)\rho}$ – internal energy of polytropic gas mass unit with adiabatic index γ, $\mathbf{q}=\{q_i\}$ – heat flow vector with its components $q_i=kT_{,j}+\tau_{ik}\upsilon_k$, T – temperature, k – thermal-conductivity coefficient; $d\Omega$ – volume element of Ω_G; dS – surface element of $\partial\Omega_G$. In (1), the first term is rate of change **Q** in volume Ω_G, the second term is conditioned by a transfer of **Q** through the boundary $\partial\Omega_G$, the third term is associated with action of external forces on the boundary $\partial\Omega_G$.

In the finite time interval $[t, t+\Delta t]$, derivative with respect to time in (1) is written as:

$$\frac{d}{dt}\int\limits_{\Omega_G[t]}\mathbf{Q}(t)d\Omega\approx\frac{1}{\Delta t}\left(\int\limits_{\Omega_G[t+\Delta t]}\mathbf{Q}[t+\Delta t]d\Omega-\int\limits_{\Omega_G[t]}\mathbf{Q}[t]d\Omega\right), \tag{3}$$

where, corresponding point in time is indicated in the brackets […].

Volumes $\Omega_G[t+\Delta t]$ and $\Omega_G[t]$ are connected by the relation:

$$\Omega_G[t+\Delta t]=\Omega_G[t]+\delta\Omega_G(t,\Delta t), \tag{4}$$

where, $\delta\Omega_G$ – integration volume is connected with boundary movement $\partial\Omega_G(t)$. Then, expression (4) enables to write the right-hand side of (3) as:

$$\int\limits_{\Omega_G[t+\Delta t]}\mathbf{Q}[t+\Delta t]d\Omega-\int\limits_{\Omega_G[t]}\mathbf{Q}[t]d\Omega=\int\limits_{\Omega_G[t]}\mathbf{Q}[t+\Delta t]d\Omega-\int\limits_{\Omega_G[t]}\mathbf{Q}[t]d\Omega+\int\limits_{\delta\Omega_G}\mathbf{Q}[t+\Delta t]d\Omega. \tag{5}$$

In view of (3) and (5), equation (1) could be transformed into:

$$\frac{1}{\Delta t}\left(\int\limits_{\Omega_G[t]}\mathbf{Q}[t+\Delta t]d\Omega-\int\limits_{\Omega_G[t]}\mathbf{Q}[t]d\Omega\right)+\int\limits_{\partial\Omega_G[t]}\mathbf{Q}(t)(\mathbf{v}\cdot\mathbf{n})dS$$
$$+\int\limits_{\partial\Omega_G[t]}\mathbf{H}(t)\cdot\mathbf{n}\,dS+\frac{1}{\Delta t}\left(\int\limits_{\delta\Omega_G}\mathbf{Q}[t+\Delta t]d\Omega\right)-\int\limits_{\partial\Omega_G[t]}\mathbf{Q}(t)(\mathbf{v}_\Gamma\cdot\mathbf{n})dS=0. \tag{6}$$

Within the limits of $\Delta t \to 0$ equation (6) is:

$$\frac{\partial}{\partial t}\int\limits_{\Omega_G[t]} \mathbf{Q}(t)d\Omega + \int\limits_{\partial\Omega_G[t]} \mathbf{Q}(t)(\mathbf{v}\cdot\mathbf{n})dS + \int\limits_{\partial\Omega_G[t]} \mathbf{H}(t)\cdot\mathbf{n}\,dS + \left\{\lim_{\Delta t\to 0}\left(\frac{1}{\Delta t}\left(\int\limits_{\delta\Omega_G} \mathbf{Q}[t+\Delta t]d\Omega\right)\right) - \int\limits_{\partial\Omega_G[t]} \mathbf{Q}(t)(\mathbf{v}_\Gamma\cdot\mathbf{n})dS\right\} = 0. \quad (7)$$

For vector $\mathbf{Q}(t)$

$$\lim_{\Delta t\to 0}(\mathbf{Q}[t+\Delta t]) = \mathbf{Q}[t]. \quad (8)$$

In addition, volume element $d\Omega \in \delta\Omega_G$ is:

$$d\Omega = \Delta t(\mathbf{v}_b\cdot\mathbf{n})dS. \quad (9)$$

Then, taking into account (8) and (9), the expression in curly brackets (7) is as:

$$\frac{d\Omega_G}{dt} - \int\limits_{\partial\Omega_G[t]} (\mathbf{v}_b\cdot\mathbf{n})dS = 0. \quad (10)$$

As a result, equation (1) written for moving volume (Lagrangian approach) is transformed into the equation for fixed volume in time for t (Eulerian approach):

$$\frac{\partial}{\partial t}\int\limits_{\Omega_G[t]} \mathbf{Q}(t)d\Omega + \int\limits_{\partial\Omega_G[t]} \mathbf{Q}(t)(\mathbf{v}\cdot\mathbf{n})dS + \int\limits_{\partial\Omega_G[t]} \mathbf{H}(t)\cdot\mathbf{n}\,dS = 0, \quad (11)$$

with initial condition $\mathbf{Q}(t{=}0,\mathbf{r}){=}\mathbf{Q}_0(\mathbf{r})$, $\mathbf{r}\in\Omega_G$ and means that (10), where $\mathbf{Q}_0$ is the initial vector. If velocity distribution $\mathbf{v'}(\mathbf{r},t)$ is specified on the movable boundary, the boundary condition in the transformation to immovable boundary is as follows:

$$\mathbf{v}(\mathbf{r},t){=}\mathbf{v'}(\mathbf{r},t){+}\mathbf{v}_b(\mathbf{r},t),\ \mathbf{r}\in\partial\Omega_G, \quad (12)$$

where $\mathbf{r}$ – radius vector of point on $\partial\Omega_G$; $\mathbf{v}(\mathbf{r},t)$ – velocity vector on immovable boundary; $\mathbf{v'}(\mathbf{r},t)$ – velocity vector on movable boundary.

Thus, the volume $\Omega_G(t)$ and boundary $\partial\Omega_G(t)$ are supposed to be immovable at time point t within time interval dt, whereas, the boundary movement itself could be considered by the boundary conditions in (12). Transformation from (1) to (11) could be explained by the fact that the point in Ω_G, takes the boundary movement through velocity, which is induced by this movement. Nevertheless, this velocity could be induced not only by the boundary movement, but also the gas injection from immovable boundary (figure 1) as expressed in (12). In the following time point, it is necessary to take into consideration the deformation of boundary $\partial\Omega_G$ under condition in (10).

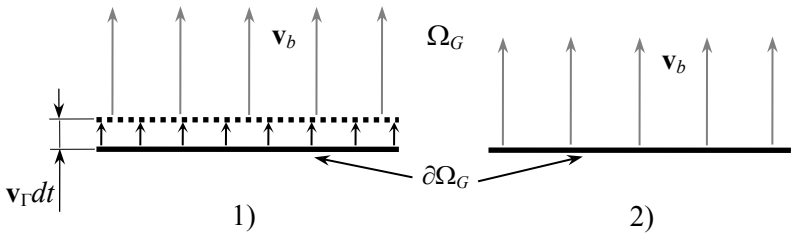

Figure 1. Velocity induced in volume Ω_G within $\partial\Omega_G$: 1) movable boundary; 2) injection from boundary.

Solid body movement within domain Ω_S, is described by geometrically nonlinear system equation:

$$\left.\begin{array}{c} \rho_S \ddot{\quad} \quad \left(\delta_{ij}+u_{i,j}\right)\Big)_{,k} \\ \varepsilon_{ij}=(1/2)\left(u_{i,j}+u_{j,i}+u_{l,i}u_{l,j}\right) \\ \sigma_{ij}=\sigma_{ij}(\varepsilon_{lm}) \end{array}\right\}, \tag{13}$$

with initial and boundary conditions:

$$\left.\begin{array}{c} \mathbf{u}(t=0,\mathbf{r})=\mathbf{u}_0(\mathbf{r}),\ \mathbf{r}\in\Omega_S \\ \dot{\quad} \quad \cdot \end{array}\right\}, \tag{14}$$

$$\left.\begin{array}{c} \mathbf{u}(t,\mathbf{r})=\mathbf{u}_b(t,\mathbf{r}),\ \mathbf{r}\in\partial\Omega_S^D \\ n_k\sigma_{kj}\left(\delta_{ij}+u_{i,j}\right)=p_i^n(t,\mathbf{r}),\quad \mathbf{r}\in\partial\Omega_S^N \end{array}\right\}, \tag{15}$$

where, ρ_S – density; $\mathbf{u}$ – vector displacement of solid body point, $\mathbf{u}=\{u_1,u_2,u_3\}$; $\mathbf{u}_0$ и – initial displacement vector and velocity of solid body point; σ_{ij} and ε_{ij} – components of stress and strain tensors; $\partial\Omega_S^D$ and $\partial\Omega_S^N$ boundary segments $\partial\Omega_S$ where Dirichlet (displacement) and Neumann (stress) conditions are imposed, $\partial\Omega_S=\partial\Omega_S^D\cup\partial\Omega_S^N$; $\mathbf{u}_b$ – vector of boundary displacements; $\mathbf{p}^n$ – load vector on surface point designated by normal vector $\mathbf{n}$.

Continuity conditions of velocity and stress on the boundary Γ are imposed for conjugation in solving problems:

$$\mathbf{v}_b(t,\mathbf{r})= \quad :\Gamma, \tag{16}$$

$$\boldsymbol{\sigma}(t,\mathbf{r})=\boldsymbol{\tau}(t,\mathbf{r}),\ \mathbf{r}\in\Gamma. \tag{17}$$

3. Algorithm solution of conjugate problem

3.1 Algorithm description

Point of time t, $\mathbf{Q}_{[t]}$, $\mathbf{u}_{[t]}$, and boundary $\Gamma_{[t]}$. are known. It is assumed that individual non-conjugate problems with initial conditions $\mathbf{Q}_{[t]}$, $\mathbf{u}_{[t]}$, in time interval $[t, t+\Delta t]$ and within domain Ω_G and Ω_S could be solved. Then, the algorithm solution of conjugate problem in time interval $[t, t+\Delta t]$ is:

1. Gas flow problem within domain $\Omega_{G[t]}$ with initial conditions $\mathbf{Q}_{[t]}$, and condition in (16) within $\Gamma_{[t]}$ is solved;
2. Values $\boldsymbol{\tau}_{[t+\Delta t]}(\mathbf{r}),\ \mathbf{r}\in\Gamma$ are defined;
3. Elasticity problem within domain $\Omega_{S[t]}$ initial conditions $\mathbf{u}_{[t]}$, and condition in (17) within $\Gamma_{[t]}$;
4. Vectors $\mathbf{u}_{[t+\Delta t]}(\mathbf{r})$ and are defined, where $\mathbf{r}\in\Gamma$;
5. If the condition is met, then the solution of conjugate problem at point of time $t+\Delta t$ is found. If not, go to item 1, where $\mathbf{Q}_{[t]}$ is used as the initial condition, but $\mathbf{v}_{b[t]}(\mathbf{r})= \quad \mathbf{r}\in\Gamma$;
6. Based on $\mathbf{u}_{[t+\Delta t]}(\mathbf{r})$, $\mathbf{r}\in\Gamma$ transformation of $\Gamma_{[t]}\rightarrow\Gamma_{[t+\Delta t]}$ is fulfilled, where condition in (10) is satisfied.

Two program modules are necessary for the numerical implementation of above-mentioned algorithm. One module is applied to solve the gas flow problem within domain Ω_G, while the second module-elasticity problem within domain Ω_S in the following time interval $[t, t+\Delta t]$. Numerical methods used in these modules and their direct implementation is beyond the scope. In fact, this algorithm describes the data interchange (conjugation) procedures between the two modules.

Iteration, described in item 5, is the congruence between the velocity of the boundary movement Γ and the load inducing this movement.

In numerical modeling, element mesh covers the domain Ω_G forming nodes at the intersection of mesh lines. As a result, fulfilling item 6, it is necessary to adjust not only boundary position Γ (nodes, on Γ), but also node positions in Ω_G to exclude over-deformation of the element shapes. Under conditions of limited displacement of solid body, the position of nodes within the domain Ω_G may be adjusted by the solution of elliptical equations. Under conditions of significant displacement, it should be remeshed. Subsequently, gas flow problem solution should interpolated from the previous mesh (at time point t) to the updated mesh (at time point $t+\Delta t$).

It should be noted that within the frame of the described algorithm, $\Gamma \in \Omega_G$ and $\Gamma \in \Omega_S$, interconnected with conjugation conditions (16) and (17), exist. Modeling boundary movement $\Gamma \in \Omega_G$ has a specific feature involving its discrete movement. Thus, fulfilling item 1, the boundary $\Gamma \in \Omega_G$ remains immovable, while its movement is replaced by the gas injection from domain Γ at velocity $\mathbf{v}_b$. Let's assume that extra gas mass inflows into the domain Ω_G resulting in the failure of the conservation law of mass at this stage. Then, in item 6, the position of boundary $\Gamma \in \Omega_G$. is adjusted. Displacement vector of boundary point $\Delta\mathbf{u}$ with the radius vector of $\mathbf{r} \in \Gamma$, $\Gamma \in \Omega_G$, is:

$$\Delta\mathbf{u}(\mathbf{r}) = \mathbf{u}_{[t+\Delta t]}(\mathbf{r}) - \mathbf{u}_{[t]}(\mathbf{r}) = \mathbf{v}_b(\mathbf{r}) \cdot \Delta t\,, \tag{18}$$

whereas, condition in (10) should be fulfilled. In this case, boundary Γ moves jump-wise to the position corresponding to the time point $t+\Delta t$. When the boundary moves into the new position, mass balance within domain Ω_G is reverted, as excess gas mass is beyond the domain Ω_G.

3.2 Algorithm testing

3.2.1 Adiabatic gas compression in movable piston cylinder

The problem of adiabatic gas compression in movable piston cylinder was described by the authors [11]. The above-described algorithm was applied in this case. The walls of the cylinder and piston are presumed to be inelastic. This presumption excludes the algorithm in the step which determines the deformation of the solid body itself. According to the solution results, numerical conditioned deviations to prescribed variables were determined. Specifically, under 1/3 gas compression of the initial volume, relative gas mass variation was $2.5 \cdot 10^{-4}$.

3.2.2 Fluid flow in flat channel with moveable wall

Let's consider incompressible viscous fluid (water) flow in a flat channel with moveable wall. Previously, this problem was examined only experimentally and solved numerically [3], [12]-[15]. In question, the numerical model of fluid flow in the channel was based on the geometrical and kinematic data described in above-mentioned papers. To calculate the incompressible viscous fluid flow, the program module with corresponding functionality was applied. The channel diagram is illustrated in figure 2.

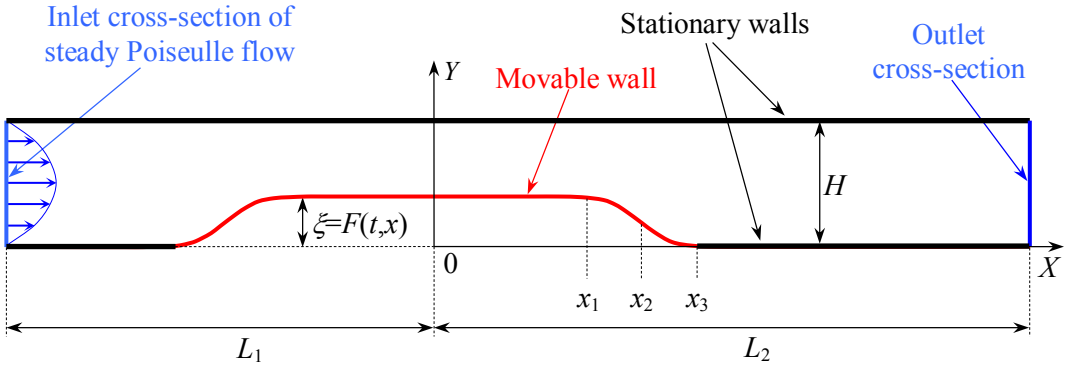

Figure 2. Плоский канал с подвижной стенкой

At initial point of time the flat channel was formed by two parallel walls, the distance being H=10^{-2} m. The remaining channel geometrical parameters are L_1=9.85H, L_2=18H, x_1=4H, x_3=6.5H, x_2=(x_1+x_3)/2. Upper channel wall is immoveable. The lower wall oscillates with time T. Distribution of non-stationary point deviations ξ=F(t,x) in lower channel wall to initial position is described as the function

$$F(t,x)=\begin{cases}\beta(t) & \text{for } 0<|x|<x_1\\ 0.5\beta(t)(1-\tanh(\alpha(|x|-x_1))) & \text{for } x_1<|x|<x_3\\ 0 & \text{for } x_3<|x|\end{cases}, \quad (19)$$

where, t – time; $\beta(t)=0.5\beta_{max}(1-\cos(2\pi\tilde{}$, $\tilde{}$, β_{max}=0.38H; α=4.14. The channel is filled with fluid, density being ρ=1000 kg/m^3 and dynamic viscosity μ=1000·10^{-6} kg/m/s.

At initial point of time, fluid flow field in the flat channel responded to steady Poiseuille flow and Reynolds number Re=$\rho V_0 H/\mu$=507, where V_0 μ is average fluid flow velocity in channel cross-section. Pressure gradient, preserving this flow, is equal to $P_{,x}$=-8$V_{max}\mu/H^2$, где V_{max}=3V_0/2. The boundary condition at inlet was assigned as parabolic velocity profile, corresponding to Poiseuille flow with given Reynolds number. At outlet boundary the pressure is P=0. No-slip condition was assigned to the upper wall, i.e. flow velocity components on the wall υ_x=υ_y=0.Velocity component υ_y on the lower wall was determined by the velocity of the boundary movement υ_y=ς . Velocity component is υ_x=0. Strouchal number is S=H/(V_0T)=0.037. Calculated fluid-filled area was meshed with quadrilateral grids, including 443×81 nodes. Integration step in time Δt=(1/3)·10^{-2}s.

Displacement of moveable wall element changes the channel shape, resulting in the formation of the vortex system as illustrated in figure 3. The vortexes are assigned alphabetic notations A, B, C, D etc.

Space mesh was adjusted in each time interval depending on the shape of the lower channel wall. Mesh fragment at initial point of time $\tilde{}$ and the same fragment $\tilde{}$ are illustrated in figure 4.

Numerically defined vortex positions B, C and D in the coordinates (X^*,$\tilde{}$ where $X^*=(10St)^{1/3}\cdot(x-x_2)/H$ are shown in figure 5. By comparison, experimental data were represented [14], as well as the numerical results from [15]. The fluid flow field behind the moveable section of the upper wall in the channel at point of time $\tilde{}$=0.4, 0.5, 0.6, 0.7 is illustrated in figure 6. The results are depicted as colored isolines of velocity components. To compare, the flow line, numerically determined under the same conditions [14] is illustrated. In this case, there exists correspondence in number, size and position of the vortexes.

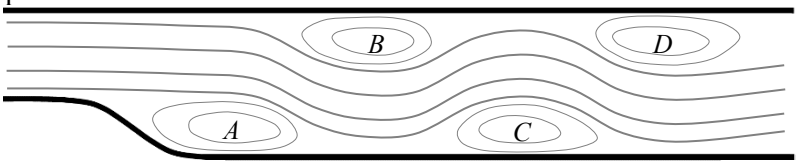

Figure 3. Fluid flow structure behind moveable wall section

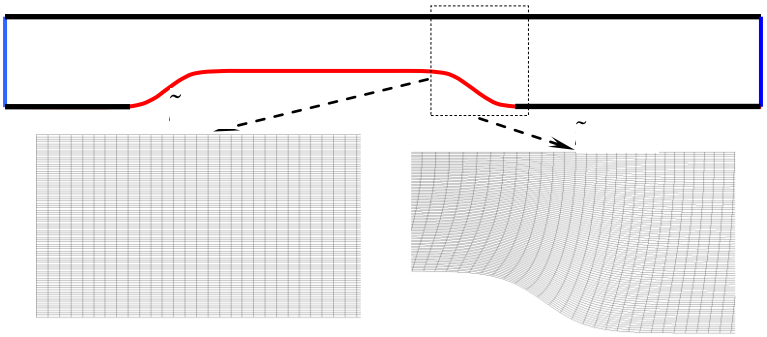

Figure 4. Mesh fragment in different points of time

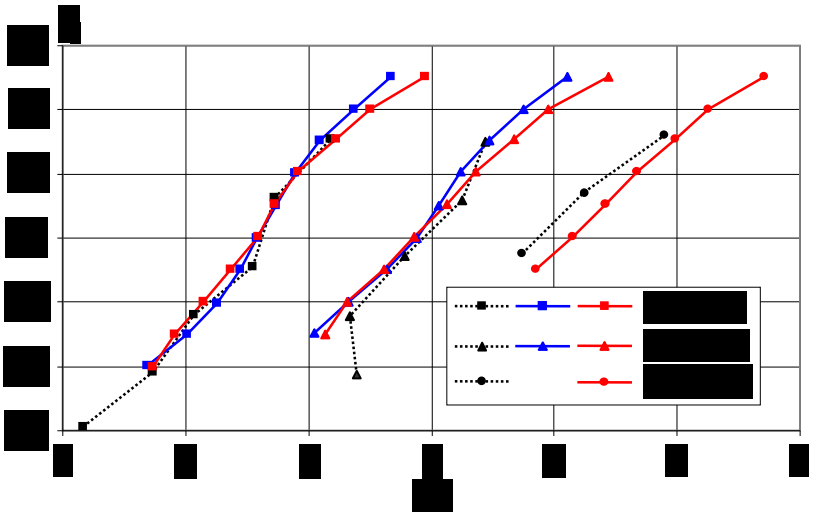

Figure 5. Vortex positions *B*, *C* and *D* in time: ····· experiment [14], —— numerical results [15], —— present numerical results

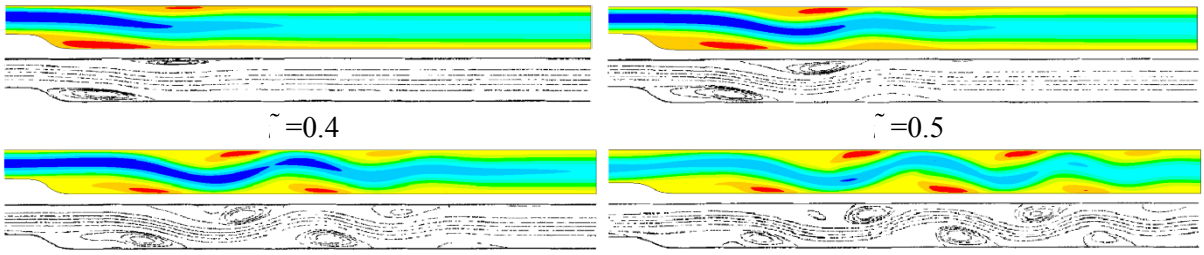

Figure 6. Fluid flow field behind moveable element in the channel: colored isolines of velocity components υ_x; black-white flow lines [14]

3.2.3 Hydroshock in elastic pipe

Pipeline section (figure 7), where fluid (water) flow, is considered. Pipeline section length L=15 m, outer pipe diameter R, wall thickness h. Fluid flow velocity in pipeline V_0=1 m/s. Physico-mechnical material characteristics are shown in table 1, while physical fluid characteristics – in table 2. Pipeline cross-section parameters which were applied in solving the conjugate problem are represented in table 3.

At point of time t=0 the channel was instantly closed by the shut-off valve, located in point x=L. Initial and boundary conditions: fluid velocity vector components $\upsilon_x(x,r,t=0)=V_0$, $\upsilon_r(x,r,t=0)=0$, $\upsilon_x(x=0,r,t)=V_0$, $\upsilon_x(x=L,r,t)=0$; pressure $P(x,r,t=0)=0$; vector components of displaced solid body $u_x(x,r,t=0)=0$, $u_r(x,r,t=0)=0$, $u_x(x=0,r,t)=0$, $u_x(x=L,r,t)=0$; velocity vector components of solid body $\dot{u}$ $0)=0$, $\dot{u}$ $0)=0$; stress $\sigma_{rx}(x=0,r,t)=0$, $\sigma_{rx}(x=L,r,t)=0$.

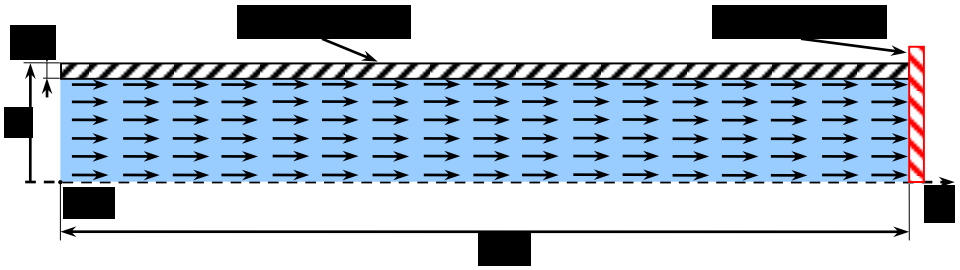

Figure 7. Problem diagram illustrating hydroshock in pipeline with flowing fluid

Table 1. Physico-mechanical characteristics of pipe material

Density, kg/m^3	7000
Elastic modulus, Pa	$9.81\cdot10^{10}$
Poisson ratio	0.3

Table 2. Physical characteristics of water

Density, kg/m^3	1000
Dynamic viscosity, kg/m/s	$1000\cdot10^{-6}$
Bulk modulus, Pa	$2.2\cdot10^9$

Finite element mesh, covering the calculated fluid-filled area, included from 600×20 nodes (large R) to 2000×20 nodes (small R). Solid body finite element mesh – from 600×3 nodes to 2000×3 nodes. Integration step in time $\Delta t=1\cdot10^{-5}$s.

To calculate weakly compressible fluid flow, the program module with corresponding functionality was applied. Based on the numerical calculation results, the velocity of the pressure jump in the pipeline a_{pipe} and pressure jump value P_{pipe} were determined. These numerical values were compared to the values obtained from the analytical expressions (Joukowski formulas for hydroshock [16])

$$a_{pipe} = a_w / \sqrt{1 + 2R \cdot E_w / (E \cdot h)}, \tag{20}$$

$$\Delta P_{pipe} = \rho_w a_{pipe} V_0, \tag{21}$$

where, a_w – sound velocity in water, a_w=1435м/с; ρ_w – water density; E_w – bulk modulus of water; E – elasticity modulus of pipe material; R – outer pipe radius ; h – pipe wall thickness.

Values a_{pipe} and ΔP_{pipe}, numerically obtained and values obtained by Joukowski formulas (20),(21) as well as corresponding relative errors $\varepsilon_{a_{pipe}}$ и $\varepsilon_{\Delta P_{pipe}}$ are presented in table 3. Numerical values a_{pipe} and ΔP_{pipe} are in good agreement with analytical calculation results. Thus, the error $\varepsilon_{a_{pipe}}$ was slightly more than 1,5%, while error $\varepsilon_{\Delta P_{pipe}}$ not more than 2%.

Table 3. Numerical and analytical values of a_{pipe} and ΔP_{pipe}, ratio errors $\varepsilon_{a_{pipe}}$ and $\varepsilon_{\Delta P_{pipe}}$

D=2R, mm	h, mm	a_{pipe}, m/s		$\varepsilon_{a_{tube}}$, %	ΔP_{pipe}, Pa		$\varepsilon_{\Delta P_{tube}}$, %
		formula (20)	num. solution		formula (21)	num. solution	
50	7.0	1339.4	1359.7	1.511	1339421	1366200	1.999
150	9.5	1245.8	1260.0	1.137	1245833	1269400	1.892
300	12.5	1173.0	1180.0	0.598	1172989	1193000	1.706
600	18.0	1103.9	1103.3	0.054	1103921	1122200	1.656

4. Discussion and results

Axisymmetric SPRE model includes casing with back bottom and front bottom. Front bottom is connected to nozzle cluster. SPRE casing consists of filler with inner channel. Casing and filler is not rigid and deforms under the pressure of the gas in the channel. Nozzle contour is not deformable. Basic dimensions are illustrated in figure 8.

Non-deformed line is illustrated as points in figure 8. It includes nozzle contour and part of front bottom contour. In determining stress-strain state of SPRE, boundary condition of zero displacement $\mathbf{u}(x,r,t)=0$ is imposed on the part of front bottom contour.

Filler combustion is modeled by gas injection from the free surface of the filler. Free filler surface area embraces 3.015 m^2 (non-deformed channel). Gas inflow from the combustion surface is – 215.17 kg/s. Gas parameters: specific heat capacity (*Cp*) – 2052.4 J/kg/K; heat conductivity – 0.41567 W/m/K; viscosity – $9.8879 \cdot 10^{-5}$ kg/m/s; molar mass – 27.944 kg/kilomole; gas constant – 297 J/kg/K; adiabatic index – 1.169549; gas temperature (of combustion products) – 3400°K. Material characteristics of SPRE structure elements are described in table 4.

Table 4. Material physical-mechanical characteristics of SPRE structure elements

	Elasticity module, Pa	Poisson ratio	Density, kg/m^3
Filler	$10 \cdot 10^6$–$20 \cdot 10^6$	0.497	2100
Casing	$37 \cdot 10^9$	0.3	1930
Back bottom	10^{12}	0.3	1930
Front bottom	10^{12}	0.3	1930

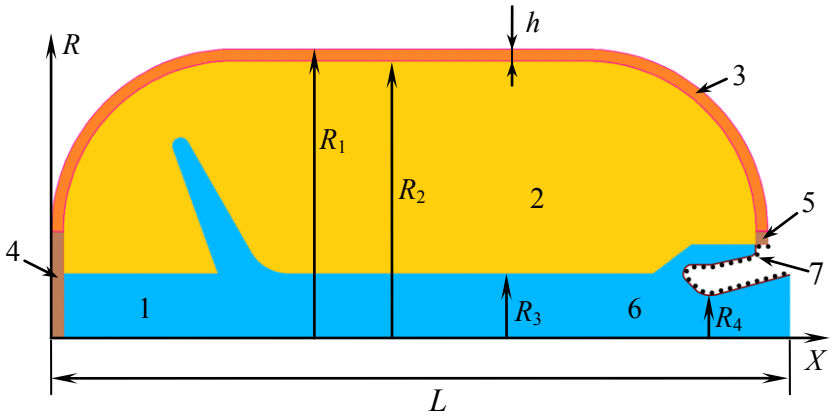

Figure 8. SPRE diagram: 1) channel; 2) filler; 3) casing; 4) back bottom; 5) front bottom; 6) nozzle contour; 7) rigid fixing area (for numerical model). R_1=0.680 m, R_2=0.650 m, R_3=0.15225 m, R_4=0.1015 m, L=1.720 m, h=0.03 m.

The mesh covering calculated areas of solid body and channel is demonstrated in figure 9. As is clear from figure 9, mesh lines are linked on the medium BI. This approach in mesh generation significantly simplifies the calculation process. However, mesh line continuity on the fluid-solid body boundary results in the over-concentration of solid-body mesh, particularly, in the contact area of that mesh covering the boundary layer of the nozzle contour.

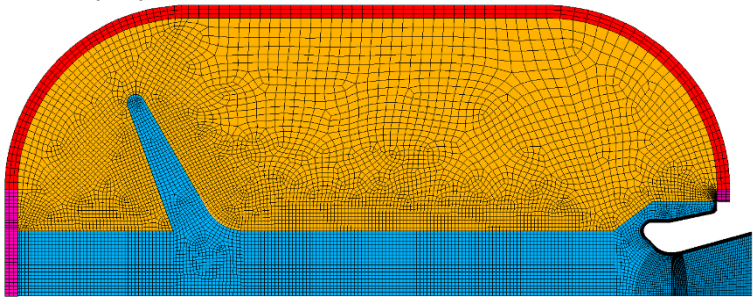

Figure 9. Mesh coverings for different areas in SPRE numerical. models

Time integration step was 10^{-5}s.

The calculation results are represented in figures 10-14.

Pressure calculation results at SPRE back bottom for different filler elasticity modules are illustrated in the graph figure 10. The curves show that the lower the filler elasticity module, the higher the steady gas pressure. This could be explained by the fact that the channel deforms when exposed to gas pressure (figure 11). In this case, the channel area increases, resulting in the mass increase of gas inflowing from the channel surface. In these conditions, the umbrella-shaped indent expands significantly in the filler, while the radius of the cylindrical channel section, located between the umbrella-shaped indent and nozzle, increases. Decreasing filler elasticity module increases the deformation of the channel, especially within the umbrella-shaped indent.

Figure 12 illustrates the (ΔR) change in time of channel radii in the filler (R_1) and outer radius of engine casing (R_3) at section $x=L/2$. Calculation results showed that under gas pressure in the channel values R1 and R3 increase within the time interval Δt =0.04 s, which further indicate oscillations near equilibrium values. This behavior is specific for the radius R_3. Decreasing filler elasticity module from 20 MPa to 10 MPa results in the redistribution of the gas-pressure load from the filler to the engine casing. This causes R3 increase to 6 mm, while R_1 to 0.2 mm.

Figures 13 and 14 illustrate the displacements (u_x) and velocity distributions (υ_x) at SPRE back bottom depending on time for filler elasticity modules E=20 MPa and E=10MPa. As seen on the graphs, back bottom displacement to a new equilibrium state is observed at the initial time interval (t < 0.04 s) under gas pressure. In the following time intervals, back bottom oscillates near equilibrium state.

It should be noted that although changes of the filler elasticity module affect $u_x(t)$ and $\upsilon_x(t)$ dependencies; however, these dependencies are close in values. Thus, in both cases, at t > 0.04 s, back bottom oscillates at the average displacement value is u_x, i.e. about 16 mm and average zero velocity. Maximal displacement velocity is 2.5 m/s for E=20 MPa and 2.7 m/s for E=10 MPa. Oscillation periods near equilibrium state are $1.372\cdot10^{-2}$s and $1.395\cdot10^{-2}$s, respectively.

Weak effect of filler elasticity module value on $u_x(t)$ and $\upsilon_x(t)$ dependencies could be explained by the existing umbrella-shaped indent. In this case, the filler becomes weak as a rigid element in the engine construction. As a result, the casing stiffness determines SPRE axial stiffness.

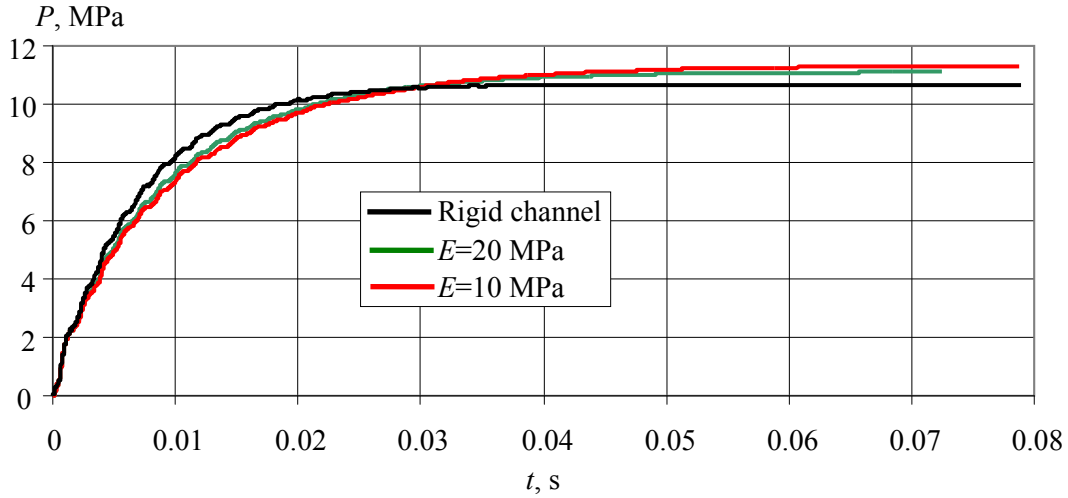

Figure 10. Gas pressure within SPRE back bottom depending on time for different filler elasticity modules E

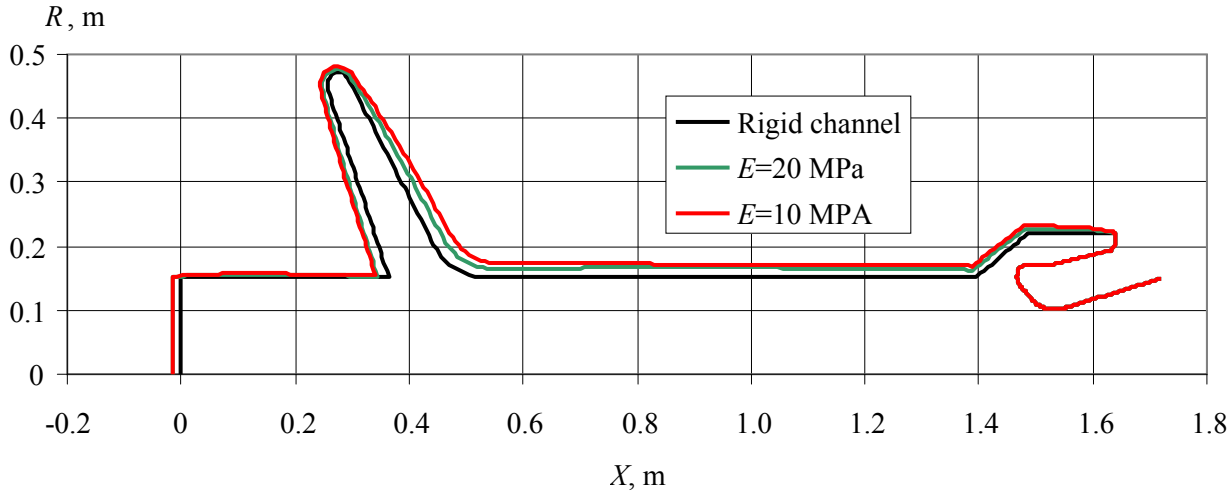

Figure 11. SPRE channel profile under different filler elasticity modules E, at time point $7.25 \cdot 10^{-2}$ s.

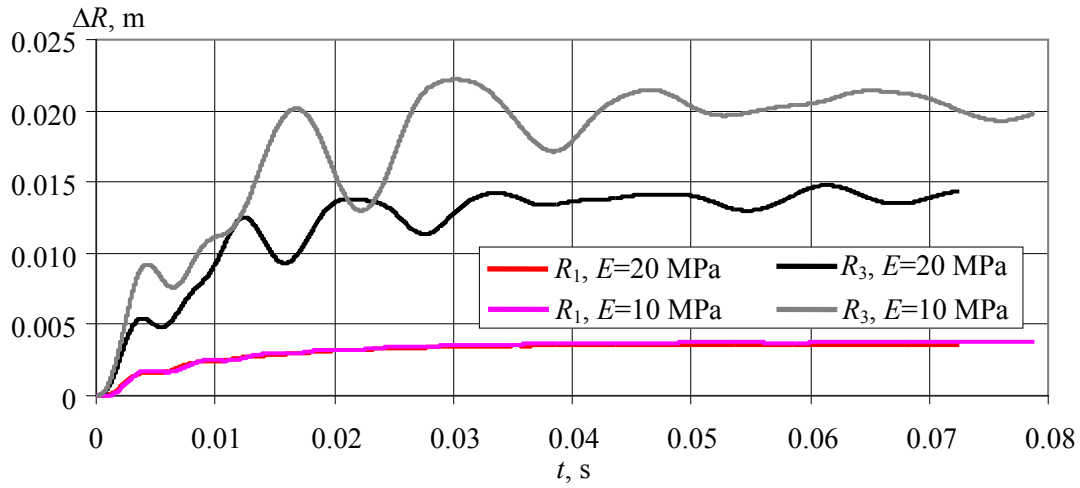

Figure 12. Changes of radii R_1 and R_3, at $x=L/2$, E=20 MPa, E=10 MPa.

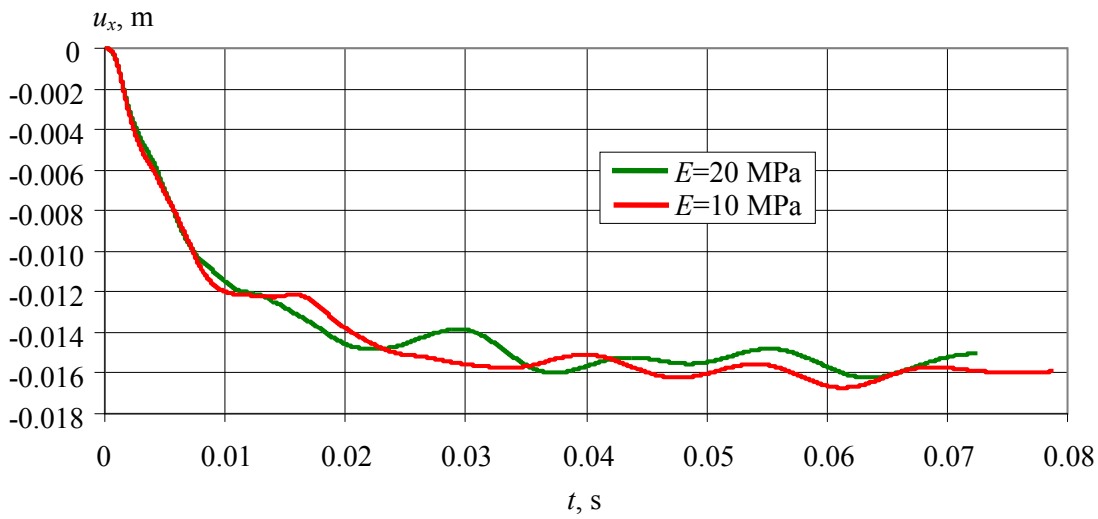

Figure 13. Displacement of the back bottom

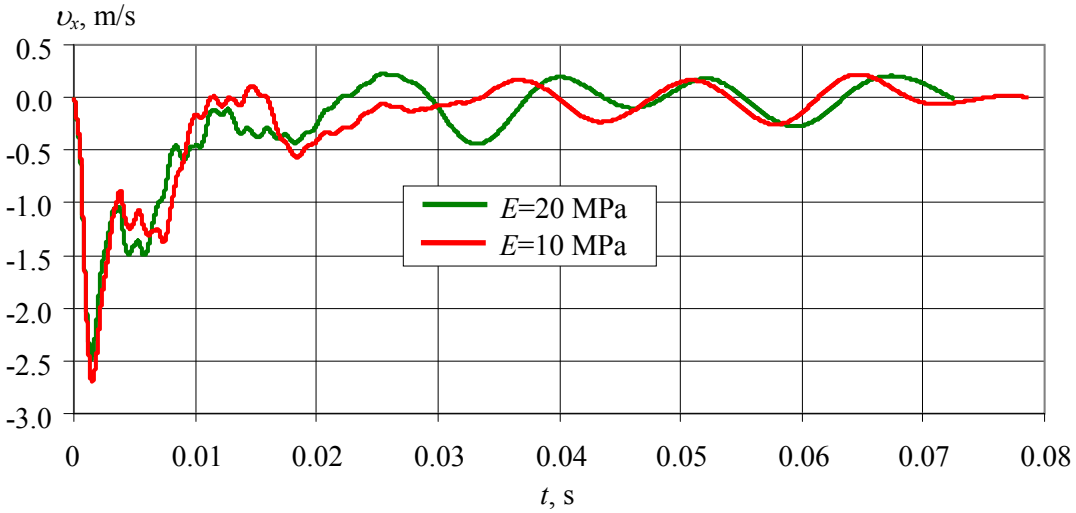

Figure 14. Displacement velocity of the back bottom

5. Conclusion

Based on the calculation results of conjugate problems for gas- solid body system, the dynamic behavior of SPRE model was considered. Dependencies $P(t)$ in the filler channel, including the SPRE construction and gas flowing in the channel interaction, were obtained. SPRE model construction deformation was estimated within radial and axial directions considering the channel shape and the filer physical-mechanical characteristics.

Acknowledgments

The results were obtained within the framework of government contract of the Ministry of Education and Science of the Russian Federation, project № 9.9063.2017/8.9.

Notifications

SPRE – solid-propellant rocket engine.
BI – boundary interface.

References

[1] Kumar M and Kuo K 1981 *AIAA J.* **19**(12) 1580–9
[2] Milekhin Yu M, Klychnikov A N, Popov V S and Melnikov V P 2012 *Combust., Expl. Shock Waves* **48**(1) 33-40
[3] Engel M and Griebel M 2006 *Int. J. Numer. Meth. Fluids* **50** 437–68
[4] Fiedler R, Jiao X, Namazifard A, Haselbacher A, Najjar F and Parson I 2001 *AIAA-2001-3954*
[5] Fiedler R, Breitenfeld M, Jiao X, Haselbacher A, Geubelle P, Guoy D and Brandyberr M 2002 *AIAA-2002-431*
[6] Kai Yang, Pengtao Sun, Lu Wang, Jinchao Xu and Lixiang Zhang 2016 *Comput. Methods Appl. Mech. Engrg.* **311** 788–814
[7] Rider W, Love E, Wong M, Strack O, Petney S and Labreche D (2011) *Int. J. Numer. Meth. Fluids* **65** 1325–37
[8] Garelli L (2011) *Fluid Structure Interaction using Arbitrary Lagrangian Eulerian Formulation* (Tesis de Doctorado, Facultad de Engeniería y Ciencias Hídricas, Universidad Nacional del Litoral, Argentina) p 146
[9] Chiravalle V P and Morgan N R 2017 *Int. J. Numer. Meth. Fluids* **83** 642–63
[10] Ozdemir Z, Moatamedi M, Fahjan Y and Souli M 2009 **3**(3) *Int. Jnl. of Multiphysics* 307-36

[11] Zhukov A P, Belov1 S V and Ponomarev S V 2019 *IOP Conf. Series: Journal of Physics: Conf. Series* **1145** 012053
[12] Stephanoff K, Pedley T, Lawrence C and Secomb T 1983 *Nature* **305** 692–5
[13] Pedley T and Stephanoff K 1985 *J. Fluid Mech.* **160** 337–67
[14] Ralph M and Pedley T 1988 *J. Fluid Mech.* **190** 87–112.
[15] Sheu T and Chen Y 2007 *Int. J. Numer. Meth. Engng* **69** 2247–63
[16] Vil'ner YA M, Kovalev YA T and Nekrasov B B 1976 *Spravochnoe posobie po gidravlike, gidromashinam i gidroprivodam* ed B B Nekrasov (Minsk: Vyshejsh. shkola) p 416 (in Russ)